Lab on a Chip

PAPER

View Article Online
View Journal | View Issue

Cite this: *Lab Chip*, 2021, **21**, 3942

Microfluidic mass transfer of CO_2 at elevated pressures: implications for carbon storage in deep saline aquifers†

Tsai-Hsing Martin Ho, Junyi Yang and Peichun Amy Tsai *

Carbon capture and sequestration (CCS) in a deep saline aquifer is one of the most promising technologies to mitigate anthropologically emitted carbon dioxide. Accurately quantifying the mass transport of CO_2 at pore-scales is crucial but challenging for successful CCS deployment. Here, we conduct high-pressure microfluidic experiments, mimicking reservoir conditions up to 9.5 MPa and 35 °C, to elucidate the microfluidic mass transfer process of CO_2 at three different states (*i.e.*, gas, liquid, and supercritical phase) into water. We measure the size change of CO_2 micro-bubbles/droplets generated using a microfluidic T-junction to estimate the volumetric mass transfer coefficient (k_La), quantifying the rate change of CO_2 concentration under the driving force of concentration gradient. The results show that bubbles/droplets under high-pressure conditions reach a steady state faster than low pressure. The measured volumetric mass transfer coefficient increases with the Reynolds number (based on the liquid slug) and is nearly independent of the injection pressure for both the gas and liquid phases. In addition, k_La significantly enlarges with increasing high pressure at the supercritical state. Compared with various chemical engineering applications using millimeter-sized capillaries (with typical k_La measured ranging from ≈0.005 to 0.8 s^{-1}), the microfluidic results show a significant increase in the volumetric mass transfer of CO_2 into water by two to three orders of magnitude, *O* (10^2–10^3), with decreasing hydrodynamic diameter (of ≈50 μm).

Received 9th February 2021,
Accepted 13th April 2021

DOI: 10.1039/d1lc00106j

rsc.li/loc

1 Introduction

The technology of CCS in saline aquifers is one of the most promising options to store a large volume of anthropologic CO_2 captured from major emission sites due to the abundant storage capacity (estimated to be greater than 10^3 Gt).[1,2] Understanding the dissolution and mass transfer of CO_2 in the pore fluid (water or brine) is critical because these processes affect the storage capacity of the early trapping mechanisms (*i.e.*, structural and residual trapping) as well as the long term solubility trapping and mineralization with the host rock.[3,4] In addition, CO_2 is a sustainable "green" solvent widely utilized in cleaning, drying, and extraction, particularly the supercritical state due to its low viscosity and surface tension with a high diffusivity.[5]

Conventional methods of measuring CO_2 dissolution rates and mass transfer include bubble column reactors[6,7] and stirred vessels.[8] A bubble column consists of a cylindrical vessel with a gas distributor at the bottom. The gas is sparged in the form of bubbles into a liquid phase or a liquid–solid slurry.[9,10] Stirred vessels usually have similar configurations to bubble columns, but they are equipped with an additional stirrer and motor to enhance the mixing and increase the interfacial area.[11] However, the drawbacks of these methods include considerable back mixing in the collecting tank, bubble coalescence, and requirement of relatively large operation space and fluid volume[6,8] and, hence, motivate efficient alternative approaches.

Microfluidics has offered emerging and promising platforms for a variety of energy and environmental technologies.[12–16] To name a few, microfluidics has been beneficially utilized for visualizing the multiphase flow patterns of viscous fingering during the gas–liquid and liquid–liquid displacement in a porous medium[16–18] as well as measuring the mass transfer rates of CO_2 (ref. 19–22) and ozone,[23] gas diffusivity in different solvents,[24] and CO_2 solubility (under the temperature effect,[25] under surfactant influence,[26] and in different solvents[22,24]).

Very recently, high-pressure microfluidic platforms have been developed to investigate the behaviors of CO_2 with a background fluid at high pressure and temperature to simulate the conditions of deep saline formations, which

Department of Mechanical Engineering, University of Alberta, Edmonton, Alberta, T6G 1H9 Canada. E-mail: peichun.amy.tsai@ualberta.ca

† Electronic supplementary information (ESI) available: Supporting data and thermodynamic parameters. See DOI: 10.1039/d1lc00106j

typically have the pressure (P) range of 6 MPa $< P <$ 27 MPa and the temperature (T) range of 26 °C $< T <$ 110 °C.[27] For example, the investigations using high-pressure microfluidics have focused on the flow patterns of CO_2 displacing fluid,[28,29] the applications of CO_2 in oil recovery processes,[30,31] physical properties (*e.g.*, density and viscosity) at the supercritical state,[32] fast screening of the CO_2 phase state in different solvents,[33,34] and solubility of CO_2 in brine.[35]

Nevertheless, microfluidic experimental studies regarding the CO_2 transport rate in water or brine under P–T conditions close to or under reservoir conditions are relatively limited.[36–39] Sell *et al.* applied a sodium fluorescein tracer to measure the diffusivity of CO_2 in brine (up to 5 M) at a pressure ranging from 0.1 to 5 MPa using a PMMA microfluidic cell. They reported that the salinity had a significant impact on the CO_2 diffusivity, while the system pressure seemed to have a minor effect on the measured diffusion coefficient.[36] Yao *et al.*[37] performed microfluidic T-junction experiments and found a gradual increase in the mass transfer coefficient, k_L (from 1.8×10^{-4} to 5.3×10^{-4} m s^{-1}), of CO_2 bubbles in water with rising pressure (from P = 0.1 to P = 3 MPa). In 2017, Yao *et al.* investigated the influence of elevated pressure on CO_2 absorption in water and a chemical solvent DEA (diethanolamine) by adjusting P ranging from 0.1 to 4 MPa. They reported a decrease in k_La with rising pressure in both physical and chemical absorption processes due to the shrinkage of the interfacial area at high pressure.[38] Qin *et al.* experimentally estimated the mass transfer coefficient k_L to be $1.5 \times 10^{-4} < k_L < 7.5 \times 10^{-4}$ m s^{-1} for supercritical CO_2 in water (at P = 8 MPa and T = 313 K), based on the three-dimensional morphology of a shrinking Taylor bubble in a rectangular channel.[40] Additionally, the results showed that a higher water volume fraction results in a larger k_L, and a faster-moving droplet generally has a higher k_L.[39]

In this study, we experimentally investigated the influence of different thermodynamic states on the microfluidic CO_2 mass transfer, which is not fully addressed in the literature, particularly the supercritical state. A CO_2 bubble/droplet was generated in a T-junction microchannel under various conditions ranging from the standard state (P = 0.1 MPa and T = 24 °C) to reservoir conditions (P = 9.5 MPa and T = 35 °C). The mass transfer rate is characterized by the volumetric mass transfer coefficient, k_La, extracted from the length change of a CO_2 slug when traveling in a microchannel. The influence of pressure on the mass transfer rate was examined. We further investigate other key parameters that may affect the mass transfer rate, such as the capillary number (Ca) and the Reynolds number (Re), and compare them with other existing experimental results, which used different hydrodynamic diameters.

2 Materials and methods

We experimentally generated CO_2 bubbles/droplets in Milli-Q water using T-junction microfluidics[41,42] and measured the size change of traveling CO_2 to acquire the mass transfer data. Microchannels were fabricated using silicon wafers and bound with a cover glass after applying the deep reactive ion etching (DRIE) technique.[43,44] Fig. 1a is an experimental snapshot illustrating the generation of CO_2 bubbles at the T-junction with an injection pressure of 1.45 MPa. The water (illustrated by the blue arrow) directly enters the main microchannel (whose width and depth are 100 μm and 30 μm, respectively) as the continuous phase, while CO_2 is injected *via* the narrower side-channel (of a width of 50 μm) to form the dispersed phase.

2.1 Experimental procedures

The microfluidics was installed in a metal platform that allows operation from standard atmospheric conditions (P = 0.1 MPa and T = 24 °C) to reservoir conditions (P = 9.5 MPa and T = 35 °C), covering the gas, liquid, and supercritical states of CO_2, as shown in Fig. 1b. A heating plate and two thermocouples (K-type) were attached to the platform to heat up and monitor the assembly's temperature, respectively. Milli-Q water was loaded in stainless steel syringes and pumped by a syringe pump (Chemyx Inc. Fusion 6000) after one hour of degassing in a vacuum chamber. CO_2 was

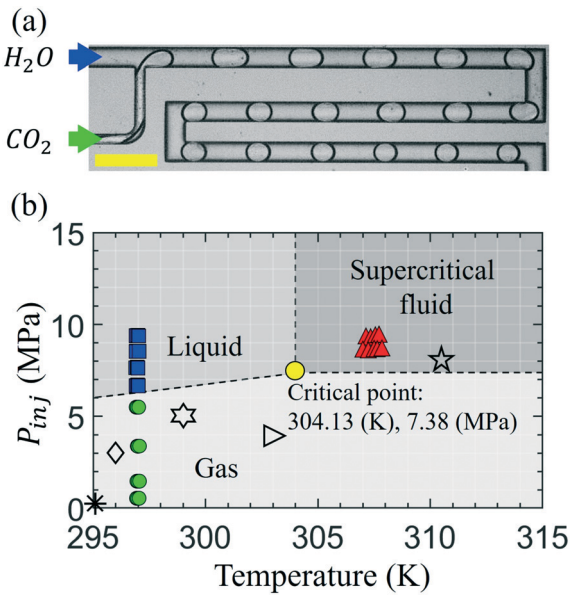

Fig. 1 (a) The snapshot of CO_2 bubbles generated using a microfluidic T-junction while subsequently moving in the channel. The water inlet has the same width as the main microchannel (100 μm), and the CO_2 channel is 50 μm in width. The depth of the microchannel is 30 μm. The (yellow) scale bar represents 300 μm. (b) The CO_2 thermodynamic phase diagram near the critical point (yellow ●). Colored symbols show our various experimental conditions for the CO_2 injection pressure, P_{inj}, facilitating different CO_2 phases: liquid (■), gas (●), and supercritical (▲). Other symbols represent the experimental conditions from previous studies, including works under atmospheric conditions (*),[19,20,23] by Sell *et al.* (✡),[36] Yao *et al.* (◊[37,45] and ▷[38]), and Qin *et al.* (☆).[39] The image of the phase diagram is adapted from the National Institute of Standards and Technology (NIST).[46]

controlled by a high-pressure gas pump (ISCO 100DX), directly connected to the gas tank (Praxair, RES K CO_2 99.998%). A backpressure regulator (TESCOM BP 25-4000PSI) was connected to the system's outlet to keep a suitable pressure gradient across the channel. The flow pattern was observed by using an inverted microscope (Zeiss Axio Observer 7 Materials) and recorded by a high-speed camera (Phantom V710L) at a rate of 5000 frames per second (fps).

2.2 Image analysis

We processed the recorded images using ImageJ (NIH Image)[47] to measure the size of a single bubble and track its position varying with time. The measured data were further analyzed by using a customized code written in Matlab (MathWorks®). The data variation was evaluated by calculating the standard deviation of at least five bubbles for each pressure condition. The results showed good consistency in both the bubble size and position. The variance is about 3% in bubble length and ≈4% in displacement.

2.3 Determining the volumetric mass transfer coefficient

As revealed by the experimental observation, *e.g.*, Fig. 1a, CO_2 bubbles gradually dissolve in water, resulting in shrinkage in size, when they move along the microchannel. We hence analyze the change of the CO_2 bubble length, L_b, with time (t) to extract the (liquid-side) volumetric mass transfer coefficient (k_La) as it moves at a speed, u_b, downstream (adjacent to a liquid slug of water with a length of L_s) in a microchannel width (d_c), schematically illustrated in Fig. 2a.

To estimate k_La, we used the so-called unit cell model[37,45,48] by analyzing the mass transfer between one single bubble and its adjacent liquid slug, illustrated by the red dotted-line compartment in Fig. 2a. Assuming that the liquid slug is initially free from CO_2 and in time CO_2 gradually dissolved while well-mixed in the adjacent liquid slug, based on the mass balance concept, the mass transfer of CO_2 from the bulk phase (bubble) through the phase boundary to the liquid slug can be mathematically described by

$$\dot{M}_{CO_2} = -\frac{\rho dV_b}{dt} = V_L \frac{dc}{dt}, \quad (1)$$

where V_L and V_b are the volumes of the liquid slug and CO_2 bubble/drop, respectively. The CO_2 density, ρ, is assumed to be a constant. The volume of the liquid slug V_L remains unchanged because of the fixed water injection rate (Q_L = 15 μl min^{-1}). c denotes the CO_2 concentration in a liquid slug as a function of position (x) and time (t). Here, the unit-cell model also assumes no mass transfer between different unit cells.[37,48]

Eqn (1) correlates the CO_2 concentration changes in a fluid element to the decrease in the bubble volume. As CO_2 bubbles/droplets move, fluid elements (in the liquid slug) repeatedly move from the bulk fluid phase onto the phase boundary (coming into contact with CO_2) and stay for a limited time, δt. The process is schematically illustrated in Fig. 2b, showing CO_2 concentration variation in the liquid bulk and along the phase boundary. The initial concentration of CO_2 in a liquid element equals that in the bulk fluid phase, denoted as $c(x)$, varying with the downstream location (x) as the CO_2 bubble/drop travels downstream. Due to the direct contact, the phase boundary (at y = 0) is always saturated with CO_2, whose saturation concentration is denoted as c^* (P,T) as a function of P and T. In short, these boundary conditions at the phase boundary and the liquid bulk can be expressed as $c(y = 0) = c^*$ and $c_\infty \equiv c(y \approx \infty) = c(x)$, respectively.

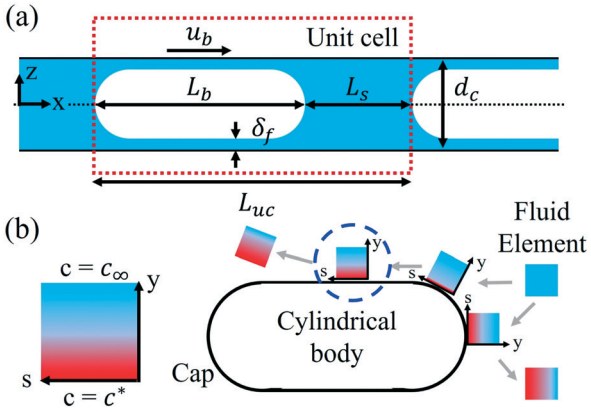

Fig. 2 The schematic of the theoretical, conceptual model: (a) a unit cell. The x-axis denotes the downstream location of a bubble after being released from the T-junction. L_{uc}, the length of a unit cell, is the sum of L_b and L_s, where L_b and L_s represent the length of the CO_2 bubble/drop and liquid plug, respectively. A bubble is surrounded by the thin liquid film of δ_f in thickness. It travels at a velocity of u_b in a microfluidic channel of the width of d_c. (b) Higbie's penetration theory:[49] a fluid element from the bulk phase may come into contact with the phase boundary at a finite time. During this period, the mass transfer is assumed only *via* molecular diffusion at the interface. The s-axis represents the streamline direction, and the y-axis denotes the mass transport direction of CO_2, which is normal to the streamline.

The mass transfer rate from a CO_2 bubble to the surrounding liquid is the integral of the mass flux through a fluid element over the surface area of the phase boundary around a bubble, A_b:

$$\dot{M}_{CO_2} = \int_{cs} J_{CO_2} dA_b = k_L A_b (c^* - c_\infty). \quad (2)$$

The CO_2 mass flux, J_{CO_2}, can be further expressed using the mass transfer coefficient, k_L, which by definition is determined by the ratio of CO_2 mass flux to the concentration gradient.

The rate change of CO_2 concentration in a liquid slug equals the mass transfer of CO_2 through the phase boundary; we therefore combine eqn (1) and (2):

$$\frac{dc}{dt} = k_L \frac{A_b}{V_L} (c^* - c(x)) = k_L a (c^* - c(x)), \quad (3)$$

where a is the specific area and defined by the ratio of A_b to V_L. The prefactor k_La in eqn (3) is the volumetric mass

transfer coefficient, an important measure for the CO_2 transport efficiency in a unit cell.

By integrating (3) and using the chain rule of total time-derivative, the CO_2 concentration change in a liquid slug can be modeled by:

$$c^* - c(x) = (c^* - c_0)\exp\left(-\frac{k_L a}{j_L}x\right), \quad (4)$$

where c_0 is the initial concentration of CO_2 in water, $c_0 \equiv c_\infty$ ($t = 0$). j_L is the superficial velocity of liquid, that is, $j_L = Q_L/A$, the ratio of the liquid injection rate (Q_L) to the cross-sectional area of the microchannel (A).

Eqn (4) describes the concentration difference with an exponential decay at a rate of $k_L a/j_L$. Substituting eqn (4) into eqn (3), the change of bubble size (or length) relates to the concentration change of liquid slugs ($\Delta c = c^* - c_0$) and $k_L a$:

$$\rho\frac{DV_b}{Dt} = \rho A_c u_b \frac{dL_b}{dx} = -k_L a V_L (c^* - c_0)\exp\left(-\frac{k_L a}{j_L}x\right). \quad (5)$$

Here, A_c is the cross-sectional area of a CO_2 bubble and assumed to be a constant. L_b denotes the bubble length, changing with the downstream position, x.

By integrating eqn (5) and dividing by the initial bubble length (L_{b0}), the dimensionless size (or length) change of a moving (CO_2) bubble with the position away from the origin (T-junction) is described by:

$$\frac{L_{b0} - L_b}{L_{b0}} = \frac{1}{L_{b0}}\frac{j_L V_L}{A_c u_b \rho}\frac{1}{(c^* - c_0)}\left[1 - \exp\left(-\frac{k_L a}{j_L}x\right)\right]. \quad (6)$$

The first term of the prefactor determines the maximum size change at the equilibrium state, and the second one ($k_L a/j_L$) determines the speed to reach equilibrium. Eqn (6) is used to obtain $k_L a$ from the size change of bubbles in a microfluidic system without measuring the concentration change in liquid slugs.[37,45] We extracted $k_L a$ using a best nonlinear fit of eqn (6) with our data measured at elevated CO_2 injection pressures to investigate the influence of pressure on the CO_2 mass transfer, *i.e.*, $k_L a$.

3 Results and discussion

3.1 CO_2 bubble/droplet size change at different phases

Our experiments were operated from gas (P_{inj} = 0.25, 1.45, 3.45, and 5.45 MPa) to liquid (P_{inj} = 6.45, 7.5, 8.5, and 9.5 MPa at room temperature) and supercritical (P_{inj} = 8.5 and 9.5 MPa at 35 (±0.5) °C) states of CO_2 to reveal the dynamics of CO_2 transfer in water and the influence of pressure. For each injection pressure, we conducted the experiments at least three times independently to check the reproducibility. In total, thirty-four sets of experimental data were summarized and presented in this work. The complete experimental data are shown in Fig. S1 in the ESI.† Revealed in Fig. 3a are representative snapshots (taken from five fixed, downstream locations along the channel), including the T-junction's origin point. The initial length of CO_2 bubbles/droplets (L_{b0}) was controlled within 212 (±7) μm, with the length of liquid slugs being 194 (±11) μm and the mean CO_2 bubble/droplet speed being 0.33 (±0.07) m s^{-1}.

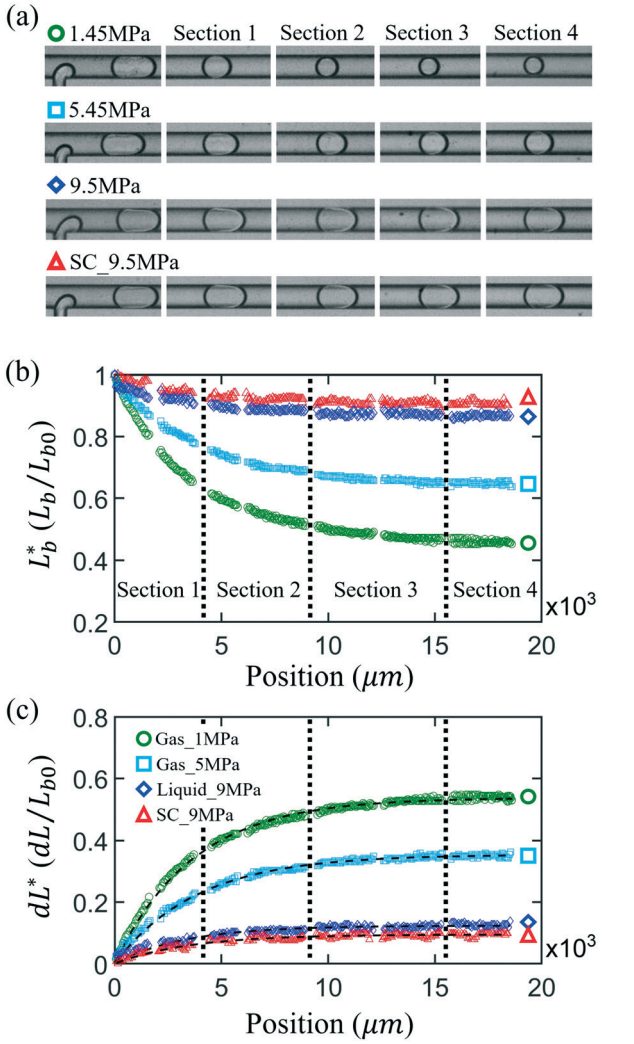

Fig. 3 (a) Experimental snapshots of CO_2 bubbles or droplets in water in the microchannel for four different injection pressures, covering the CO_2 phase state from gas (○ and □) to liquid (◇) and supercritical state (△). As a reference of scale, the width of the channel is 100 μm. CO_2 bubbles/droplets shown in (a) correspond to different locations: at the initial position (x = 0), 4000 μm (section 1), 9000 μm (section 2), 15 000 μm (section 3), and 18 600 μm (section 4) away from the T-junction. Dimensionless length and length change of the CO_2 bubbles/droplets measured from the image sequences are shown in (b) and (c), respectively. In (c), the comparison of the measured CO_2 length change with the results of nonlinear regression fitting of the simplified form of eqn (6): $dL^* = \alpha(1 - \exp(-\beta x))$ is shown. The volumetric mass transfer coefficient, $k_L a$, is obtained by multiplying the fitting coefficient, $\beta = k_L a/j_L$, by the inlet water flux, j_L.

Fig. 3b and c show the dimensionless length, $L_b^* = L_b/L_{b0}$, and dimensionless length change, $dL/L_{b0} = 1 - L_b/L_{b0}$, of CO_2 *vs.* the traveling distance recorded from (a), respectively. It is noteworthy that all CO_2 bubbles/droplets experienced a rapid shrinkage when they departed from the T-junction and later reached a final steady state. Under high-pressure conditions, the size change became subtle. As seen in Fig. 3b, CO_2

bubbles shrank more than half of their initial length at low system pressure (*e.g.*, 1.45 MPa depicted by ○). As the pressure increased, the range of drastic size change became smaller, shown by the data of 5 MPa (depicted by □). In the liquid (◇) and supercritical state (△), the shrinkage of a droplet decreased to about 10% of its initial length. Meanwhile, these high-pressure CO_2 drops reached the final steady-state size faster than the low-pressure ones. It took 12 ms on average for liquid and supercritical CO_2 droplets to reach a final steady state, whereas the CO_2 bubbles at 1 MPa needed more than 30 ms to reach their stable size.

To examine the above distinct observations, we correlated the dimensionless maximum size change of CO_2 (dL^*_{max}) with the CO_2 density, $\rho(P,T)$, bubble velocity, u_b, and liquid volume fraction, v_{slug}, measured from experiments to investigate their influences on the (quasi-)equilibrium size (see section 2 in the ESI†). The dL^*_{max} was determined using the mean value of dL^* in the plateau region of Fig. 3c. The results showed that the CO_2 density has a strong but negative correlation with its size change. The significant difference in size change at the different states is likely attributed to the increase in CO_2 density with increasing P, as it transforms from the gas, to liquid, and to supercritical state. For instance, the CO_2 density increases by ≈25×, rising from ρ = 28.19 to 693.95 Kg m^{-3}, when P increases from P = 1.45 MPa to P = 9.5 MPa for the same T = 24 °C, as shown in Table S1 in the ESI.† Although the CO_2 solubility in water, *i.e.*, $c^* - c_0$, also increases with pressure, this solubility increase (by ≈3×, from 21.86 Kg m^{-3} at 1.5 MPa (ref. 50) to ≈67.3 at 9.63 MPa (ref. 51)) is smaller than the contribution from the increase in CO_2 density.

The bubble velocity and the liquid volume had only a minor influence on the size change of gas CO_2 ($P \leq 6.29$ MPa). The influences of these two parameters (for the ranges explored) are negligible when the CO_2 phase changed to liquid and supercritical CO_2 (as shown in Fig. S2 in the ESI†).

3.2 Volumetric mass transfer coefficient, k_La, under elevated pressure

We extracted the volumetric mass transfer coefficient, k_La, by applying a nonlinear regression method with a reduced form of eqn (6): $Y = \alpha(1 - \exp(\beta X))$, to fit the experimental data of dependent variable Y as a function of parameter X, which is the downstream location x from the T-junction. Fig. 3c reveals the dimensionless size-change of CO_2 dL^*/L_{b0} under different pressure conditions and the resultant fitting of the nonlinear regression (depicted by the black dashed lines). Overall, eqn (6) models well our experimental data. At the gas states ($P \leq 6.29$ MPa), the R-squared values were between 0.97 and 0.99. The standard deviation of fitting coefficients was smaller than 1% for the prefactor α and within 3.2% for the mass transfer coefficient term β. For the results in the liquid and supercritical CO_2 phases, the uncertainty of α increased to 5% and 10–15% for the error of β. The larger percentage errors in the latter cases are associated with the experimental resolution (corresponding to ≈4 μm per pixel) and due to the relatively smaller change in the CO_2 size in the high-P regime. In addition, a close examination of CO_2 bubble/droplet geometry shows a slightly asymmetric shape as we measure a difference of 1 μm between the front and rear spherical radii of CO_2. Using eqn (6) and calculating the corresponding change in A_c, we estimate that this asymmetric CO_2 shape would contribute ≈5% error in k_La.

The data reveals that the majority of CO_2 transports in the rapid shrinkage stage at the initial time, as seen in section 1 in Fig. 3, especially for high-pressure cases. We hence focused on this short period (about 9 ms) to highlight the influence of pressure on CO_2 mass transfer in water. Fig. 4 shows the resultant volumetric mass transfer coefficient, k_La, in the rapid shrinkage stage and the data from previous experiments,[19,20,23,37,39] which primarily focused on low pressures. As seen in the figure, k_La does not change significantly for low injection pressure when P_{inj} is smaller than 8 MPa, with an average k_La = 28.85 s^{-1}. When P_{inj} raises to above 8 MPa, k_La increases to 45.4 s^{-1} on average for liquid CO_2 and greatly enlarges to a mean value of 100 s^{-1} for supercritical CO_2. Our data reveal that the average volumetric mass transfer coefficient, k_La, is increased from the gas, liquid, to supercritical state for a comparative CO_2 traveling speed (of $u_b \approx 0.33$ m s^{-1}) in a microfluidic channel. This significant gain in k_La for the supercritical state may be primarily attributed to the temperature increase, from 24 °C (room temperature) to 35 °C for a comparable u_b range in our experiments. The rising temperature activates both water

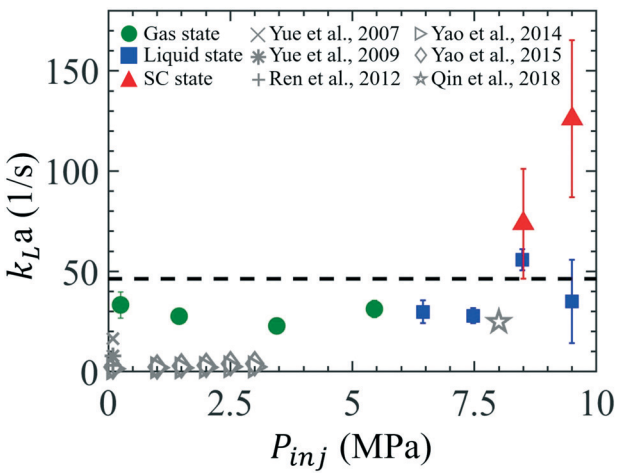

Fig. 4 The volumetric mass transfer coefficients, k_La, during the rapid shrinkage stage (section 1) against elevated injection pressures, P_{inj}. Our data span a wide range of P_{inj}, covering three different states, gas (●), liquid (■), and supercritical (▲), of CO_2. The shown points represent the average value of at least three independent experiments repeated for the same experimental conditions. Error bars denote the standard deviations. The black dashed line presents the mean value over all the presented data, $\langle k_La \rangle$ = 46.4 (s^{-1}). Grey symbols are the maximum k_La available from previous microfluidic experimental results,[19,20,23,37,39] which mostly focused on the low range of P_{inj} and used a microchannel of a size greater than 100 μm.

and CO_2 molecules and thus enhances the mass transfer processes by increasing CO_2 diffusivity. As a reference, the diffusion coefficient of CO_2 in water increases from 1.88 × 10^{-9} to 2.18 × 10^{-9} (m^2 s^{-1}) as measured in the temperature at 25 °C and 35 °C, respectively.[52]

Overall, CO_2 droplets in the rapid shrinkage stage give an average value of k_La = 46.4 (1/s) (black dashed line in Fig. 4) in a microfluidic channel of a small hydrodynamic diameter (of d_h = 46 μm). This value is greater than those from previous microfluidic data operated under lower pressure conditions (0.1–3 MPa) and at room temperature, with their k_La values ranging between 0.3 and 16 (1/s).[19,20,23,37] The k_La measured in our experiments was improved by 3× to 150× compared to those from the previous data. Since the range of CO_2 traveling speed, u_b, is comparable between the experiments, the significant increase in k_La measured in our experiments compared to previous low-P data likely comes from the larger specific area (a) created by our microchannel, as elaborated below.

The specific area, a, is conventionally defined as the ratio of the interfacial area to the volume of the two phases.[53] For a similar total volume of the two phases, a can greatly enhance the mass transfer process by increasing the contact area of the multiphase. According to the calculation proposed by Vandu *et al.*,[48] the specific area consists of two parts, namely two spherical caps and a cylindrical body of the drop or bubble (*i.e.*, CO_2), as follows:

$$a = a_{cap} + a_{body} \approx \frac{4}{L_s} + \frac{4(L_b - d_h)}{d_h L_s}. \quad (7)$$

The specific area hence is inversely related to the microfluidic hydraulic diameter, d_h.

Most of the microfluidic experiments studying the mass transfer rates for the segmented gas–liquid flow applied hydraulic diameters larger than 200 μm, which could generate bubbles with the specific area (a), calculated based on eqn (7), ranging from 3400 to 10^4 m^{-1}.[19,20,23,37] As a comparison, our microchannel has a low hydraulic diameter of 46 μm, which significantly enlarges the specific area of CO_2 bubbles/droplets up to 10^5 m^{-1} on average, approximately 10× to 30× greater than those of previous microfluidic experiments.[19,20,23,37] In addition, the recent high-pressure microfluidic experiment (with P_{inj} = 8 MPa and $T \approx$ 313 K) done by Qin *et al.*[39] found the mass transfer coefficient, k_L, to be between 1.5 × 10^{-4} and 7.5 × 10^{-4} m s^{-1}, consistent with the low-pressure regime data.[19,20,23,37] With a large specific area of 33 200 m^{-1}, this high-pressure microfluidic data also yields a large k_La up to 24.9 (s^{-1}) (depicted by ⋆),[39] consistent with our microfluidic data in the comparable pressure range. In short, these comparisons reveal that a smaller microfluidic channel enhances the volumetric mass transfer coefficient significantly by increasing the specific interfacial area, thereby benefiting various chemical reactions using a smaller h_d.

Furthermore, the mass transfer coefficient, k_L, at room temperature in this work is estimated to be 3.4 (±0.71) × 10^{-4} m s^{-1} on average. This result is consistent with the k_L reported in previous micro-scale experiments (1.8 × 10^{-4} ≤ k_L ≤ 7.3 × 10^{-4} m s^{-1}).[19,20,23,37] For supercritical CO_2, the k_L is calculated to be as high as 9.96 × 10^{-4} m s^{-1} on average, which is about three times larger than the values estimated in the gas and liquid states. The higher k_La value of supercritical CO_2 compared to the liquid/gas counterpart may be attributed to the greater temperature (35 °C) and shorter contact time of a fluid element on the CO_2–water interface. The latter is suggested by Higbie's penetration theory,[49] where the mass transfer coefficient is modeled to be proportional to the square root of diffusivity:

$$k_L \sim \sqrt{\frac{D}{\pi \tau_c}}, \quad (8)$$

where D is the diffusivity and τ_c denotes the contact of a fluid element on the CO_2–water interface. D generally has a linear correlation to temperature, reported by previous experimental[52,54,55] and simulation works.[56]

3.3 CO_2 mass transfer rate

We further investigate the influence of the Capillary number (Ca) and Reynolds number (Re) of the injected water on k_La (see Fig. 5). Here, Ca = $\mu_l \cdot u_b/\sigma$, representing the ratio of the viscous drag of the carrier liquid (*i.e.*, water) to the interfacial tension between CO_2 and water, σ. Re = $\rho_l u_b d_h/\mu_l$ is calculated by comparing the inertial force of a moving bubble to the liquid's viscous force, where ρ_l is the liquid density, u_b is the CO_2 traveling speed, and d_h is the hydrodynamic diameter of the microfluidic channel. The values of these thermodynamic parameters used are given in Tables S2 and S3 in the ESI.†

On the one hand, as shown in Fig. 5a, the volumetric mass transfer coefficient does not significantly correlate with the Capillary number, Ca, ranging from 1.9 × 10^{-3} to 1.4 × 10^{-2} in this study. The change in Ca primarily stems from the decrease in the CO_2–water surface tension (σ) as the CO_2 phase changed from gas to the supercritical state. On the other hand, we correlated the k_La with the Reynolds number in Fig. 5b, to study the influence of CO_2 velocity. As an approximation, the black dashed line represents the result of linear regression analysis from all the experimental data, showing that k_La grows linearly with a prefactor of 0.53 (±0.58) with Re.

The dependence of k_La on Re, observed from our data, indicates the significance of CO_2 bubble velocity, u_b, on enhancing the mass transfer. This observation generally agrees with approximations proposed previously, considering the bubble velocity (u_b), a critical parameter that determines k_La.[48,53,57] Illustrated in Fig. 5b inset are the empirical results of k_La found in millimeter-scale capillaries, and here we plot their data as a function of Re based on their experimental conditions. All of the empirical results show a rising k_La with increasing Re, *i.e.*, the moving speed of bubbles. This dependent relation between k_La and Re may be associated with the fact that a faster u_b enhances the mixing of fluid

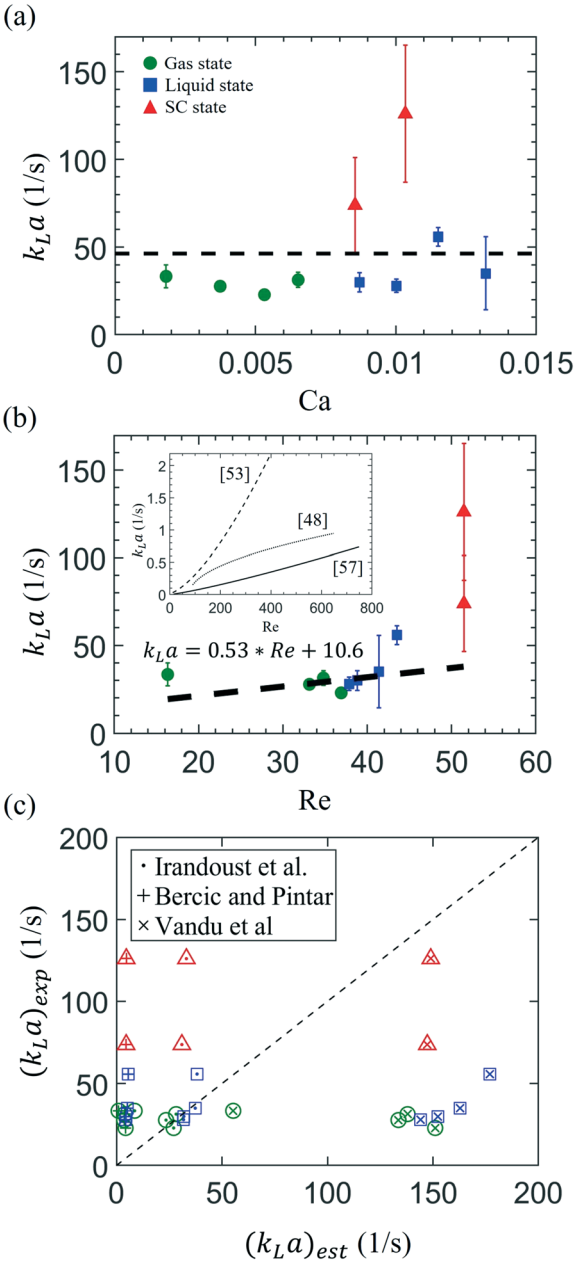

Fig. 5 The correlation of the measured volumetric mass transfer coefficient, k_La, with (a) the capillary number, Ca = $\mu_l u_b/\sigma$, and (b) the Reynolds number, Re = $\rho_l u_b d_h/\mu_l$ of the continuous liquid phase. u_b is the mean velocity of a moving bubble/droplet, and d_h denotes the hydraulic diameter of the microchannel, which is 46 μm in this study. ρ_l, μ_l, and σ represent the density and dynamic viscosity of the water and the H_2O–CO_2 interfacial tension varying with pressure, respectively. Presented in the inset are the three empirical approximations of k_La previously proposed by Irandoust *et al.*[53] [dashed line (with y_m = 0.5)], Berčič and Pintar[57] (solid line), and Vandu *et al.*[48] (dotted line). (c) The comparison of experimental data from this study, $(k_La)_{exp}$, and values estimated using the above empirical approximations, $(k_La)_{est}$, previously proposed by Irandoust *et al.* (·),[53] Berčič and Pintar (+),[57] and Vandu *et al.* (×).[48] Three different colors represent the experimental conditions in three phase states of CO_2: green color denotes the gas state, and blue and red symbols represent the conditions using liquid and supercritical CO_2, respectively.

elements on the phase boundary and the fresh bulk fluid due to the more intensive liquid slug's internal recirculation.[58,59] Also, from the perspective of Higbie's penetration theory,[49] the more intensive internal recirculation implies the more frequent contact of fluid elements with the phase boundary and the shorter contact time for a fluid element on the phase boundary, thereby increasing k_L [based on eqn (8)].

Besides the dimensionless parameters, both temperature and the viscosity of water affect CO_2 diffusion in water. Under uniform temperature conditions, the diffusivity of CO_2 is inversely proportional to water viscosity.[60] The water viscosity μ_l varies from 9.14×10^{-4} to 7.22×10^{-4} (Ns m^{-2}) as the injection pressure elevates from 0.15 MPa at room temperature up to 9.5 MPa at 35 °C. This decrease in water viscosity may lead to a 26% increase in CO_2 diffusivity in water, which may partially explain the greater k_La measured for supercritical CO_2. Studies also show that surface tension could play a role in mass transfer for a stationary micron-sized gas-bubble when the bubble radius ≲15 μm and the solvent is nearly saturated.[61,62] Under these conditions, the Laplace pressure between the two phases can enhance gas molecules' transport into the surrounding solvent due to overpressure. In our experiments, we degas water for an hour to make sure it is initially free from any dissolving gases, including CO_2. The large concentration difference between the CO_2 bubble/droplet and adjacent water would primarily drive the mass transfer of CO_2.[62] In addition, the surface tension between CO_2 and water and, hence, the Laplace pressure decreases at elevated pressure [by about three times compared to that at 1 atm (see Table S2 in the ESI†)]. Therefore, the influence of the Laplace pressure (estimated to be 1 kPa) or surface tension on the CO_2 mass transfer at elevated pressure (of P_{inj} = 9.5 MPa) is likely negligible in our cases.

How do our microfluidic results compared with the k_La obtained using the segmented gas–liquid flow (so-called Taylor flow) in millimeter-sized capillaries,[53] which are beneficially used in monolithic chemical catalyst reactors? Fig. 5c shows such a comparison between our experimental results and the k_La estimated by three empirical approximations with millimeter-scale capillaries. Our experimental results of $(k_La)_{exp}$ are plotted in the *Y*-axis, whereas the correspondingly estimated values, $(k_La)_{est}$, in the *X*-axis, by substituting our experimental conditions into the previous empirical equations, described below.

First, the semi-theoretical model developed by Irandoust *et al.* (depicted by *) considers the bubble speed (u_b) playing a crucial role in the mass transfer on both cap sides and the center cylinder of a Taylor bubble:[53]

$$k_La = 4[\delta_f(d_h - \delta_f)U_{av}\, y_m + D\,\mathrm{Sh}(d_{hc} - 2\delta_f)]/(d_h{}^2 L_{uc}), \quad (9)$$

where U_{av} is the mean velocity of the liquid film passing through the cylindrical part of a bubble, which is a function of u_b (Re). Sh denotes the Sherwood number, defined by the ratio of convective to diffusive mass transport.[63] y_m is defined

as the mix cup concentration of the solute in the liquid film (in contact with the cylindrical part of the Taylor bubble)[53] and represents the dimensionless fraction of dissolving gas in the liquid film ($0 < y_m < 1$). The higher y_m implies more solute dissolving in the solvent *via* the cylindrical part of a bubble. Previous experimental data of k_La (for $11 < Re < 824$) using millimeter-scale capillaries showed consistent results,[53] albeit ≈30% lower, compared to the (semi-) theoretical predictions. Notably, this model performs a good prediction on our results at room temperature if assuming $y_m = 0.052$, as depicted by blue and green symbols. The low y_m implies that the film contribution is small and inactive for mass transfer [see eqn (9)].

Second, results calculated using Berčič and Pintar's model underestimate the k_La compared to our measurements (depicted by +):

$$k_La = p_1 \times u_b^{p_2}/L_s^{p_3}, \quad (10)$$

where $p_1 = 0.111$, $p_2 = 1.19$, and $p_3 = 0.57$,[57] respectively. This empirical model was developed to fit the results measured from experimental conditions of long L_{b0} ($28\ mm < L_{b0} < 110\ mm$) and relatively low u_b ($0.076\ m\ s^{-1} < u_b < 0.15\ m\ s^{-1}$). In the previous experiments, the long gas bubble and slow velocity make the mass transfer from the cylindrical side of a bubble inactive, *i.e.*, corresponding to the case of $y_m = 0$ in eqn (9). Therefore, without modeling the contribution from the thin film, this model would underestimate and result in smaller k_La for our experimental conditions (as shown in Fig. 5c).

Third, the empirical model proposed by Vandu *et al.* suggests that the mass transfer happens primarily *via* the cylindrical body to the liquid film. The contribution from the cap side can be neglected because of the small specific area a of the cap side compared to the cylindrical body;[48] therefore

$$k_La = C_1\sqrt{\frac{DU_g}{L_{uc}}}\frac{1}{d_h} \approx C_1\frac{\sqrt{Du_bL_{b0}}}{L_{uc}d_h}, \quad (11)$$

where the prefactor C_1 is found to be 4.5 to fit their results the best, D is the diffusion coefficient of the solvent, and $U_g = u_b\cdot(L_{b0}/L_{uc})$. This model considering only the film contribution, however, overestimates the k_La under our experimental conditions (depicted by x). This model corresponds to another extreme condition of eqn (9) as $y_m \approx 1$, when the fluid elements on the cylindrical body remain active.

In brief, our microfluidic measurements of k_La for the segmented gas–liquid are significantly greater than those obtained by millimeter-size capillaries. Consistently, k_La generally increases with increasing u_b and, hence, Re. Compared with various empirical models developed for the millimeter-size capillaries, our microfluidic segmented Taylor flow measurements show the contributions of mass transfer from both the spherical caps and the thin liquid film.

4 Conclusions

We experimentally investigated the microfluidic CO_2 mass transfer rate in water under high-pressure conditions, ranging from the normal state on the ground (0.25 MPa and 24 °C) to the deep formation's reservoir conditions (9.5 MPa and 35 °C) for CCS applications. With the microfluidic measurements of the segmented flow's size-change in a high-pressure microfluidic device, we extracted the liquid-side volumetric mass transfer coefficient k_La to quantify the dynamic mass transport of CO_2 bubbles/droplets in gas, liquid, and supercritical states. The resultant k_La reveals a more intensive mass transfer for supercritical CO_2. The measurement of k_La also shows an approximately linear dependency on the Reynolds number of the continuous phase with a factor of 0.53. Our microfluidic results with $d_h \approx 50\ \mu m$ show a significant increase of k_La, by $O(1–10^2)$ compared to other low-pressure microfluidic measurements (with $d_h \approx 200\ \mu m$) and by $O(10^2–10^3)$ compared to those obtained using millimeter-size capillaries. Future work could extend the current parameter scope to investigate the important effect of temperature and microchannel size on microfluidic (two-phase) mass transfer, which is crucial for the technologies of microreactors and intensified extraction.

In terms of CCS applications, our experimental results revealed intensive mass transfer (k_La) of CO_2 in the supercritical state at the micro-pore scale ($d_h \approx 50\ \mu m$), leading to fast saturation in water at the early stage and benefiting subsequent sequestration of CO_2. In addition, the increase in the CO_2's traveling velocity (u_b) considerably enhances its mass transfer. These two primary outcomes can help assess the relevant time-scale and volume of supercritical CO_2's mass transfer in water for the *P–T* conditions and fluid inject rates used. Furthermore, the microfluidic platform presented can be extended for beneficial applications of microfluidic visualizations of CO_2-EOR under different reservoir conditions and intensive extractions using the green solvent supercritical CO_2.

Author contributions

Tsaihsing Martin Ho: investigation, methodology, software, formal analysis, writing – original draft, visualization. Junyi Yang: software. Peichun Amy Tsai: conceptualization, methodology, validation, software, writing – revision, visualization, supervision, funding acquisition.

Conflicts of interest

There are no conflicts to declare.

Acknowledgements

We gratefully acknowledge the support from the Canada First Research Excellence Fund (CFREF), Future Energy System (FES T02-P05 CCUS projects) at the University of Alberta, and Canada Foundation for Innovation (CFI 34546). We also thank

S. Bozic and S. Munro for their help with micro-fabrications at the nanoFAB in the University of Alberta. P. A. T. holds a Canada Research Chair (CRC) in Fluids and Interfaces and gratefully acknowledges funding from the Natural Sciences and Engineering Research Council of Canada (NSERC) and Alberta Innovates (AI), in particular the NSERC Canada Research Chairs Program (CRC 233147) and Discovery Grant (RGPIN-2020-05511).

Notes and references

1 C. M. White, B. R. Strazisar, E. J. Granite, J. S. Hoffman and H. W. Pennline, *J. Air Waste Manage. Assoc.*, 2003, **53**, 645–715.
2 S. Bachu and J. Adams, *Energy Convers. Manage.*, 2003, **44**, 3151–3175.
3 M. D. Aminu, S. A. Nabavi, C. A. Rochelle and V. Manovic, *Appl. Energy*, 2017, **208**, 1389–1419.
4 J. A. Neufeld, M. A. Hesse, A. Riaz, M. A. Hallworth, H. A. Tchelepi and H. E. Huppert, *Geophys. Res. Lett.*, 2010, **37**, 22.
5 E. J. Beckman, *J. Supercrit. Fluids*, 2004, **28**, 121–191.
6 Y. Shah, B. G. Kelkar, S. Godbole and W.-D. Deckwer, *AIChE J.*, 1982, **28**, 353–379.
7 N. Kantarci, F. Borak and K. O. Ulgen, *Process Biochem.*, 2005, **40**, 2263–2283.
8 K. Van't Riet, *Ind. Eng. Chem. Process Des. Dev.*, 1979, **18**, 357–364.
9 P. M. Wilkinson, H. Haringa and L. L. Van Dierendonck, *Chem. Eng. Sci.*, 1994, **49**, 1417–1427.
10 C. Fleischer, S. Becker and G. Eigenberger, *Chem. Eng. Sci.*, 1996, **51**, 1715–1724.
11 G. Vázquez, M. Cancela, R. Varela, E. Alvarez and J. Navaza, *Chem. Eng. J.*, 1997, **67**, 131–137.
12 J. De Jong, R. G. Lammertink and M. Wessling, *Lab Chip*, 2006, **6**, 1125–1139.
13 E. Kjeang, N. Djilali and D. Sinton, *J. Power Sources*, 2009, **186**, 353–369.
14 D. Sinton, *Lab Chip*, 2014, **14**, 3127–3134.
15 M. Abolhasani, A. Günther and E. Kumacheva, *Angew. Chem., Int. Ed.*, 2014, **53**, 7992–8002.
16 V. A. Lifton, *Lab Chip*, 2016, **16**, 1777–1796.
17 G. Bongrand and P. A. Tsai, *Phys. Rev. E*, 2018, **97**, 061101.
18 M. Saadat, P. A. Tsai, T.-H. Ho, G. Øye and M. Dudek, *ACS Omega*, 2020, **5**, 17521–17530.
19 J. Yue, G. Chen, Q. Yuan, L. Luo and Y. Gonthier, *Chem. Eng. Sci.*, 2007, **62**, 2096–2108.
20 J. Yue, L. Luo, Y. Gonthier, G. Chen and Q. Yuan, *Chem. Eng. Sci.*, 2009, **64**, 3697–3708.
21 R. Sun and T. Cubaud, *Lab Chip*, 2011, **11**, 2924–2928.
22 M. Abolhasani, M. Singh, E. Kumacheva and A. Günther, *Lab Chip*, 2012, **12**, 1611–1618.
23 J. Ren, S. He, C. Ye, G. Chen and C. Sun, *Chem. Eng. J.*, 2012, **210**, 374–384.
24 S. G. Lefortier, P. J. Hamersma, A. Bardow and M. T. Kreutzer, *Lab Chip*, 2012, **12**, 3387–3391.
25 E. Tumarkin, Z. Nie, J. I. Park, M. Abolhasani, J. Greener, B. Sherwood-Lollar, A. Günther and E. Kumacheva, *Lab Chip*, 2011, **11**, 3545–3550.
26 S. Shim, J. Wan, S. Hilgenfeldt, P. D. Panchal and H. A. Stone, *Lab Chip*, 2014, **14**, 2428–2436.
27 K. Michael, A. Golab, V. Shulakova, J. Ennis-King, G. Allinson, S. Sharma and T. Aiken, *Int. J. Greenhouse Gas Control*, 2010, **4**, 659–667.
28 C. Zhang, M. Oostrom, J. W. Grate, T. W. Wietsma and M. G. Warner, *Environ. Sci. Technol.*, 2011, **45**, 7581–7588.
29 S. Morais, N. Liu, A. Diouf, D. Bernard, C. Lecoutre, Y. Garrabos and S. Marre, *Lab Chip*, 2016, **16**, 3493–3502.
30 P. Nguyen, D. Mohaddes, J. Riordon, H. Fadaei, P. Lele and D. Sinton, *Anal. Chem.*, 2015, **87**, 3160–3164.
31 A. Sharbatian, A. Abedini, Z. Qi and D. Sinton, *Anal. Chem.*, 2018, **90**, 2461–2467.
32 B. Pinho, S. Girardon, F. Bazer-Bachi, G. Bergeot, S. Marre and C. Aymonier, *J. Supercrit. Fluids*, 2015, **105**, 186–192.
33 B. Pinho, S. Girardon, F. Bazer-Bachi, G. Bergeot, S. Marre and C. Aymonier, *Lab Chip*, 2014, **14**, 3843–3849.
34 B. Bao, J. Riordon, Y. Xu, H. Li and D. Sinton, *Anal. Chem.*, 2016, **88**, 6986–6989.
35 N. Liu, C. Aymonier, C. Lecoutre, Y. Garrabos and S. Marre, *Chem. Phys. Lett.*, 2012, **551**, 139–143.
36 A. Sell, H. Fadaei, M. Kim and D. Sinton, *Environ. Sci. Technol.*, 2013, **47**, 71–78.
37 C. Yao, Z. Dong, Y. Zhao and G. Chen, *Chem. Eng. Sci.*, 2015, **123**, 137–145.
38 C. Yao, K. Zhu, Y. Liu, H. Liu, F. Jiao and G. Chen, *Chem. Eng. J.*, 2017, **319**, 179–190.
39 N. Qin, J. Z. Wen, B. Chen and C. L. Ren, *Appl. Phys. Lett.*, 2018, **113**, 033703.
40 N. Qin, J. Z. Wen and C. L. Ren, *Phys. Rev. E*, 2017, **95**, 043110.
41 T. Thorsen, R. W. Roberts, F. H. Arnold and S. R. Quake, *Phys. Rev. Lett.*, 2001, **86**, 4163.
42 P. Garstecki, M. J. Fuerstman, H. A. Stone and G. M. Whitesides, *Lab Chip*, 2006, **6**, 437–446.
43 S. Franssila, *Introduction to microfabrication*, John Wiley & Sons, 2010.
44 T.-H. M. Ho and P. A. Tsai, *Lab Chip*, 2020, **20**, 3806–3814.
45 C. Yao, Z. Dong, Y. Zhao and G. Chen, *Chem. Eng. Sci.*, 2014, **112**, 15–24.
46 NIST, Standard Reference Database Number 69, 2020, https://webbook.nist.gov/chemistry/.
47 M. D. Abràmoff, P. J. Magalhães and S. J. Ram, *Biophotonics Int.*, 2004, **11**, 36–42.
48 C. Vandu, H. Liu and R. Krishna, *Chem. Eng. Sci.*, 2005, **60**, 6430–6437.
49 T. K. Sherwood, R. L. Pigford and C. R. Wilke, *Mass transfer*, McGraw-Hill, 1975.
50 A. Valtz, A. Chapoy, C. Coquelet, P. Paricaud and D. Richon, *Fluid Phase Equilib.*, 2004, **226**, 333–344.
51 T. Nakayama, H. Sagara, K. Arai and S. Saito, *Fluid Phase Equilib.*, 1987, **38**, 109–127.
52 A. Tamimi, E. B. Rinker and O. C. Sandall, *J. Chem. Eng. Data*, 1994, **39**, 330–332.
53 S. Irandoust, S. Ertlé and B. Andersson, *Can. J. Chem. Eng.*, 1992, **70**, 115–119.

54 B. Jähne, G. Heinz and W. Dietrich, *J. Geophys. Res.: Oceans*, 1987, **92**, 10767–10776.
55 S. P. Cadogan, G. C. Maitland and J. M. Trusler, *J. Chem. Eng. Data*, 2014, **59**, 519–525.
56 J. W. Mutoru, A. Leahy-Dios and A. Firoozabadi, *AIChE J.*, 2011, **57**, 1617–1627.
57 G. Berčič and A. Pintar, *Chem. Eng. Sci.*, 1997, **52**, 3709–3719.
58 A. Günther, M. Jhunjhunwala, M. Thalmann, M. A. Schmidt and K. F. Jensen, *Langmuir*, 2005, **21**, 1547–1555.
59 S. Kuhn and K. F. Jensen, *Ind. Eng. Chem. Res.*, 2012, **51**, 8999–9006.
60 İ. Tosun, *Fundamental Mass Transfer Concepts in Engineering Applications*, CRC Press, 2019.
61 W. Kloek, T. Van Vliet and M. Meinders, *J. Colloid Interface Sci.*, 2001, **237**, 158–166.
62 P. B. Duncan and D. Needham, *Langmuir*, 2004, **20**, 2567–2578.
63 R. Clift, J. R. Grace and M. E. Weber, *Bubbles, drops, and particles*, Courier Corporation, 2005.